

Light scattering laboratories

Jesús Escobar-Cerezo

October-December, 2018



UNIVERSITY OF HELSINKI

Experimental single scattering matrices from aerosols

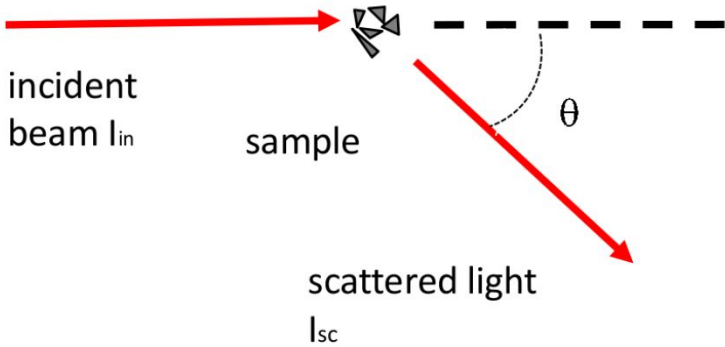
Chronological evolution

1. A new polarization-modulated light scattering instrument. **Hunt & Huffman, 1973.**
2. Measuring scattering matrices of small particles at optical wavelengths (In Mishchenko *et al.* Light scattering by nonspherical particles) **Hovenier, 2000.**
3. Experimental determination of scattering matrices of dust particles at visible wavelengths: The IAA light scattering apparatus. **Muñoz *et al.* 2010.**

Scattering matrix

$$\begin{pmatrix} I_{sc} \\ Q_{sc} \\ U_{sc} \\ V_{sc} \end{pmatrix} = \frac{\lambda^2}{4\pi^2 D^2} \begin{pmatrix} F_{11} & F_{12} & F_{13} & F_{14} \\ F_{21} & F_{22} & F_{23} & F_{24} \\ F_{31} & F_{32} & F_{33} & F_{34} \\ F_{41} & F_{42} & F_{43} & F_{44} \end{pmatrix} \begin{pmatrix} I_{in} \\ Q_{in} \\ U_{in} \\ V_{in} \end{pmatrix}$$

I_{in} → Intensity
 Q_{in} → Linear polarization
 V_{in} → Circular polarization



Scattering matrix depends on:

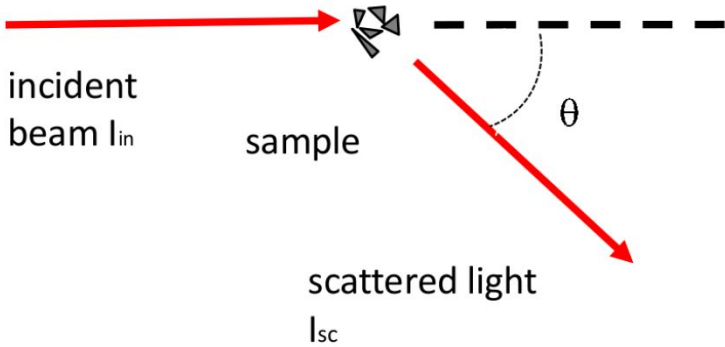
- Refractive index
- Shape
- Size distribution
- Wavelength

Size parameter

$$x = \frac{2\pi r}{\lambda}$$

Scattering matrix

$$\begin{pmatrix} I_{sc} \\ Q_{sc} \\ U_{sc} \\ V_{sc} \end{pmatrix} = \frac{\lambda^2}{4\pi^2 D^2} \begin{pmatrix} F_{11} & F_{12} & 0 & 0 \\ F_{12} & F_{22} & 0 & 0 \\ 0 & 0 & F_{33} & F_{34} \\ 0 & 0 & -F_{34} & F_{44} \end{pmatrix} \begin{pmatrix} I_{in} \\ Q_{in} \\ U_{in} \\ V_{in} \end{pmatrix}$$



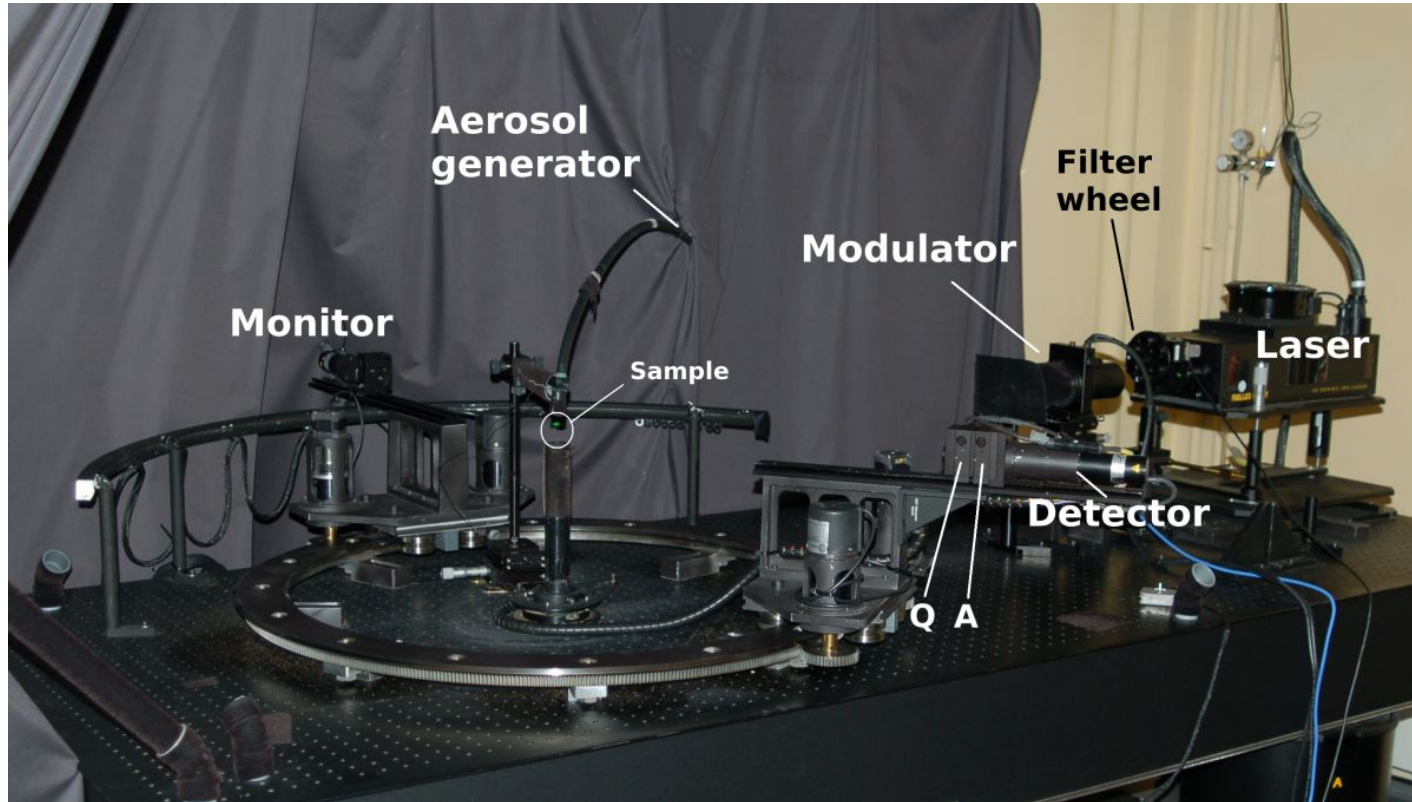
Scattering matrix depends on:

- Refractive index
- Shape
- Size distribution
- Wavelength

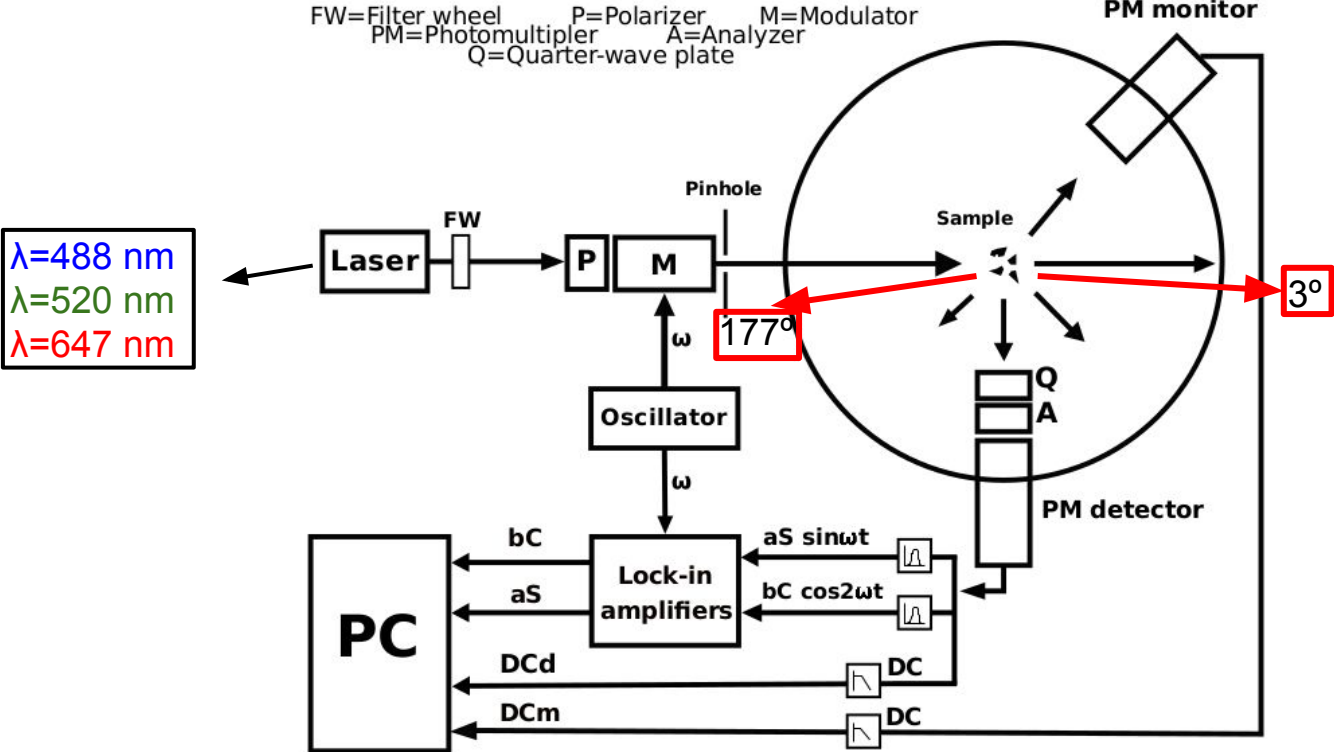
Size parameter

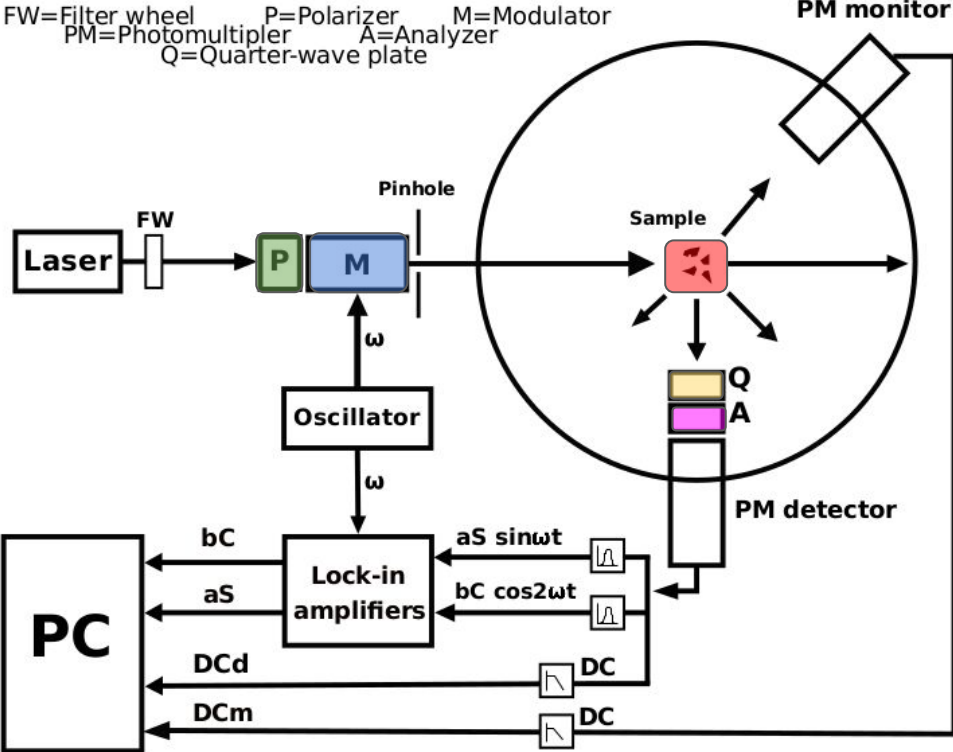
$$x = \frac{2\pi r}{\lambda}$$

IAA-CODULAB experimental apparatus.



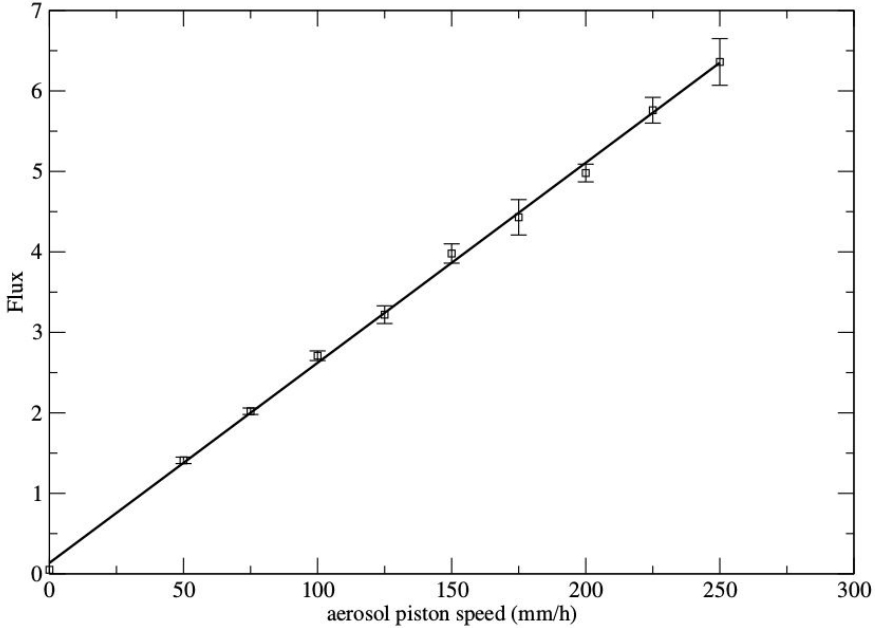
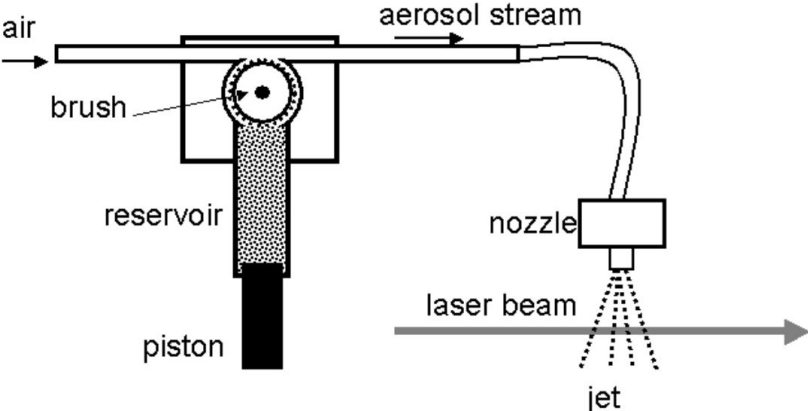
IAA-CODULAB





$$\Phi_{sca}(\lambda, \theta) = c_1 A_{\gamma_A} Q_{\gamma_Q} F(\theta) M_{\gamma_M} P_{\gamma_P} \Phi_{inc}(\lambda, \theta)$$

Aerosol generator and single scattering test.



Mueller matrices and optical configurations.

$$\Phi_{sca}(\lambda, \theta) = c_1 \mathbf{A}_{\gamma_A} \mathbf{Q}_{\gamma_Q} \mathbf{F}(\theta) \mathbf{M}_{\gamma_M} \mathbf{P}_{\gamma_P} \Phi_{inc}(\lambda, \theta)$$

$$\mathbf{A}_{\gamma} = \mathbf{P}_{\gamma} = \frac{1}{2} \begin{pmatrix} 1 & C & S & 0 \\ C & C^2 & SC & 0 \\ S & SC & S^2 & 0 \\ 0 & 0 & 0 & 0 \end{pmatrix} \quad \mathbf{Q}_{\gamma} = \begin{pmatrix} 1 & 0 & 0 & 0 \\ 0 & C^2 & SC & -S \\ 0 & SC & S^2 & C \\ 0 & S & -C & 0 \end{pmatrix}$$

$$\mathbf{M}_{\gamma_M}(\phi) = \begin{pmatrix} 1 & 0 & 0 & 0 \\ 0 & C^2 + S^2 \cos \phi & SC(1 - \cos \phi) & -S \sin \phi \\ 0 & SC(1 - \cos \phi) & S^2 + C^2 \cos \phi & C \sin \phi \\ 0 & S \sin \phi & -C \sin \phi & \cos \phi \end{pmatrix}$$

$$C = \cos 2\gamma \text{ and } S = \sin 2\gamma$$

$$\phi = \phi_c + \phi_0 \sin \omega t$$

Mueller matrices and optical configurations.

$$M_{\gamma_M}(\phi) = \begin{pmatrix} 1 & 0 & 0 & 0 \\ 0 & C^2 + S^2 \cos \phi & SC(1 - \cos \phi) & -S \sin \phi \\ 0 & SC(1 - \cos \phi) & S^2 + C^2 \cos \phi & C \sin \phi \\ 0 & S \sin \phi & -C \sin \phi & \cos \phi \end{pmatrix}$$

$$\sin \phi = \sin(\phi_0 \sin \omega t) = 2 \sum_{k=1}^{\infty} J_{2k-1}(\phi_0) \sin(2k-1)\omega t$$

$$\cos \phi = \cos(\phi_0 \sin \omega t) = J_0(\phi_0) + 2 \sum_{l=1}^{\infty} J_{2l}(\phi_0) \cos(2l)\omega t$$

Mueller matrices and optical configurations.

$$\Phi_{sca}(\lambda, \theta) = c[DC(\theta) + 2J_1(\phi_m)S(\theta) \sin \omega t + 2J_2(\phi_m)C(\theta) \cos 2\omega t]$$

Configuration	$\gamma_P(deg)$	$\gamma_M(deg)$	$\gamma_Q(deg)$	$\gamma_A(deg)$	DC(θ)	S(θ)	C(θ)
1	45	0	-	-	F_{11}	$-F_{14}$	F_{13}
2	45	0	-	45	$F_{11} + F_{31}$	$-F_{14}-F_{34}$	$F_{13}+F_{33}$
3	45	0	0	45	$F_{11} + F_{41}$	$-F_{14}-F_{44}$	$F_{13}+F_{43}$
4	0	-45	-	-	F_{11}	$-F_{14}$	F_{12}
5	0	-45	-	0	$F_{11} + F_{21}$	$-F_{14}-F_{24}$	$F_{12}+F_{22}$

$$\Phi_{sca}(\lambda, \theta) = c_1 A_{\gamma_A} Q_{\gamma_Q} F(\theta) M_{\gamma_M} P_{\gamma_P} \Phi_{inc}(\lambda, \theta)$$

Mueller matrices and optical configurations.

$$\Phi_{sca}(\lambda, \theta) = c [DC(\theta) + 2J_1(\phi_m)S(\theta)\sin \omega t + 2J_2(\phi_m)C(\theta)\cos 2\omega t]$$

Configuration	$\gamma_P(deg)$	$\gamma_M(deg)$	$\gamma_Q(deg)$	$\gamma_A(deg)$	DC(θ)	S(θ)	C(θ)
1	45	0	-	-	F_{11}	$-F_{14}$	F_{13}
2	45	0	-	45	$F_{11} + F_{31}$	$-F_{14}-F_{34}$	$F_{13}+F_{33}$
3	45	0	0	45	$F_{11} + F_{41}$	$-F_{14}-F_{44}$	$F_{13}+F_{43}$
4	0	-45	-	-	F_{11}	$-F_{14}$	F_{12}
5	0	-45	-	0	$F_{11} + F_{21}$	$-F_{14}-F_{24}$	$F_{12}+F_{22}$

$$\Phi_{sca}(\lambda, \theta) = c_1 A_{\gamma_A} Q_{\gamma_Q} F(\theta) M_{\gamma_M} P_{\gamma_P} \Phi_{inc}(\lambda, \theta)$$

Alignment example

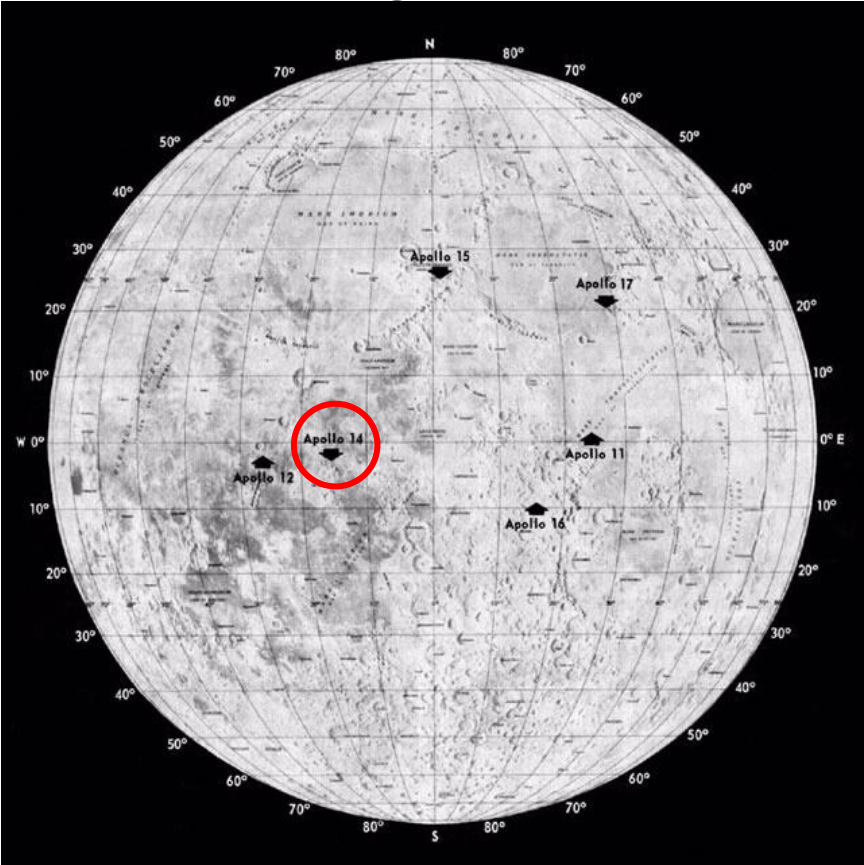
Configuration	$\gamma_P(deg)$	$\gamma_M(deg)$	$\gamma_Q(deg)$	$\gamma_A(deg)$	DC(θ)	S(θ)	C(θ)
1	45	0	-	-	F_{11}	$-F_{14}$	F_{13}
2	45	0	-	45	$F_{11} + F_{31}$	$-F_{14}-F_{34}$	$F_{13}+F_{33}$
3	45	0	0	45	$F_{11} + F_{41}$	$-F_{14}-F_{44}$	$F_{13}+F_{43}$
4	0	-45	-	-	F_{11}	$-F_{14}$	F_{12}
5	0	-45	-	0	$F_{11} + F_{21}$	$-F_{14}-F_{24}$	$F_{12}+F_{22}$

$$\Phi_{sca}(\lambda, \theta) = c_1 \mathbf{A}_{\gamma_A} \mathbf{Q}_{\gamma_Q} \mathbf{F}(\theta) \mathbf{M}_{\gamma_M} \mathbf{P}_{\gamma_P} \Phi_{inc}(\lambda, \theta)$$

$$\mathbf{I}_{sca} = \mathbf{F}(\theta) \cdot \mathbf{M}_{0^\circ} \cdot \mathbf{P}_{45^\circ} \mathbf{I}_{in} = \left(\frac{I_{in} + U_{in}}{2} \right) \begin{bmatrix} F_{11} - F_{14} \sin \phi + F_{13} \cos \phi & \text{I} \\ F_{21} - F_{24} \sin \phi + F_{23} \cos \phi & \text{Q} \\ F_{31} - F_{34} \sin \phi + F_{33} \cos \phi & \text{V} \\ F_{41} - F_{44} \sin \phi + F_{43} \cos \phi & \text{U} \end{bmatrix}$$

Experimental measurements of the JSC-1A lunar analog

JSC-1A lunar analog



Apollo landing sites (Smithsonian Institution)



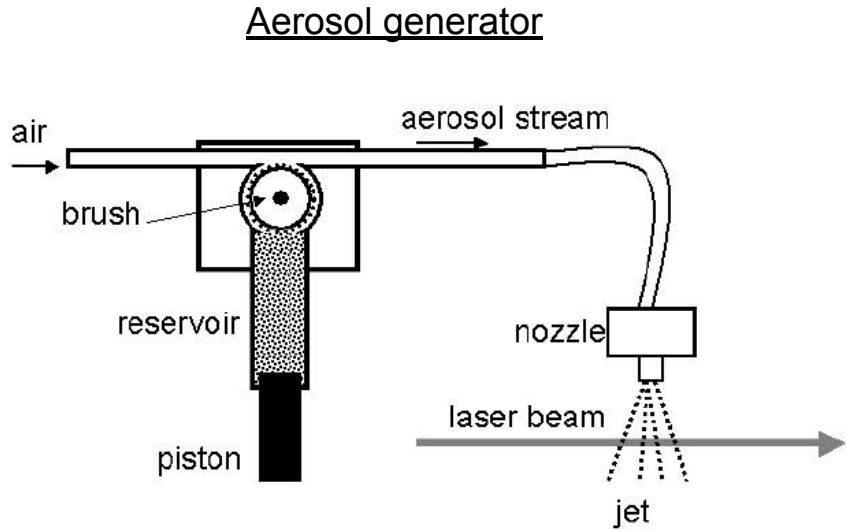
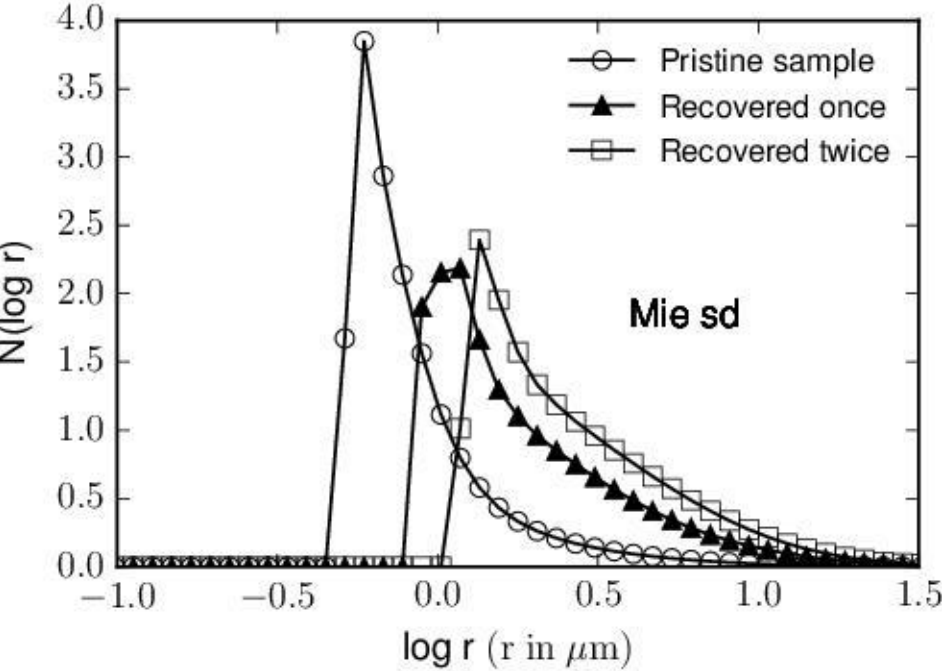
JSC-1A sample (By ArnoldReinhold - Own work, CC BY-SA 3.0)

JSC-1A lunar analog

Constituent oxides	Apollo 14 sample 14163 (Papike et al. 1982)	JSC-1A (Ray et al. 2010)
SiO ₂	47.3 %	45.7 %
Al ₂ O ₃	17.8 %	16.2 %
CaO	11.4 %	10.0 %
FeO	10.5 %	-
Fe ₂ O ₃	-	12.4 %
MgO	9.6 %	8.7 %
TiO ₂	1.6 %	1.9 %
Na ₂ O	0.70 %	3.2 %
K ₂ O	0.55 %	0.8 %
MnO	0.135 %	0.2 %

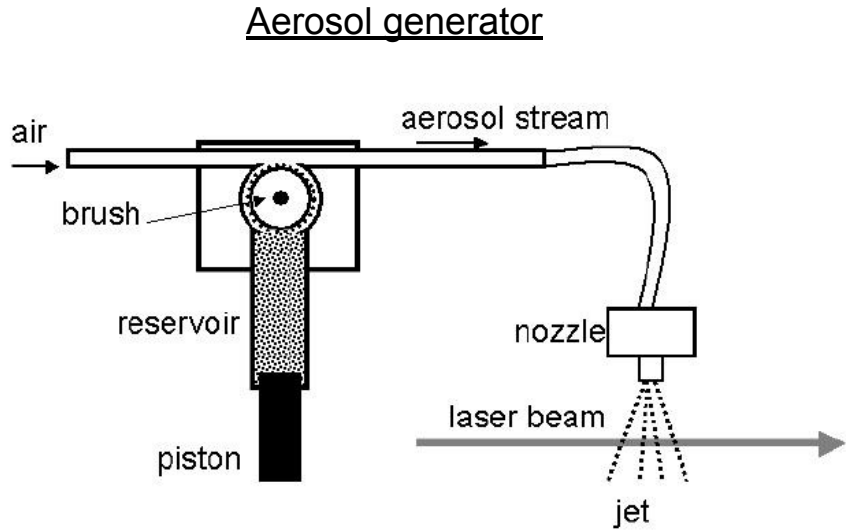
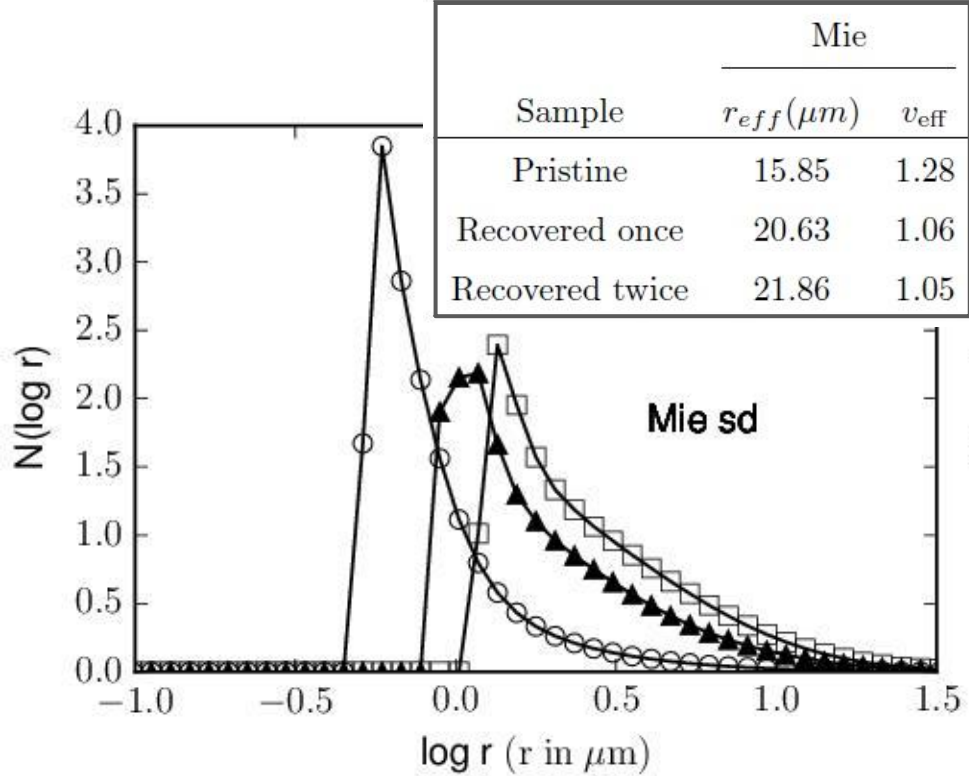
JSC-1A size distribution

Size distribution



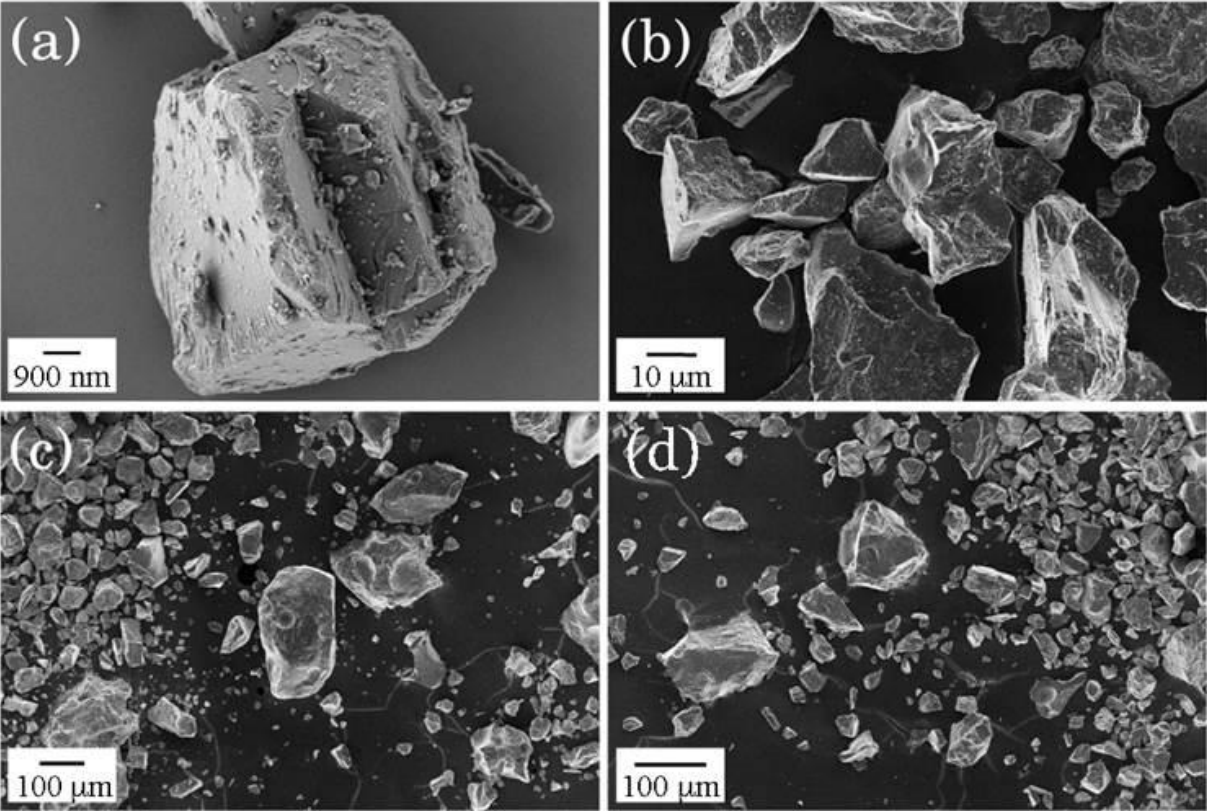
Escobar-Cerezo et al. (ApJSS, 2018)

JSC-1A size distribution



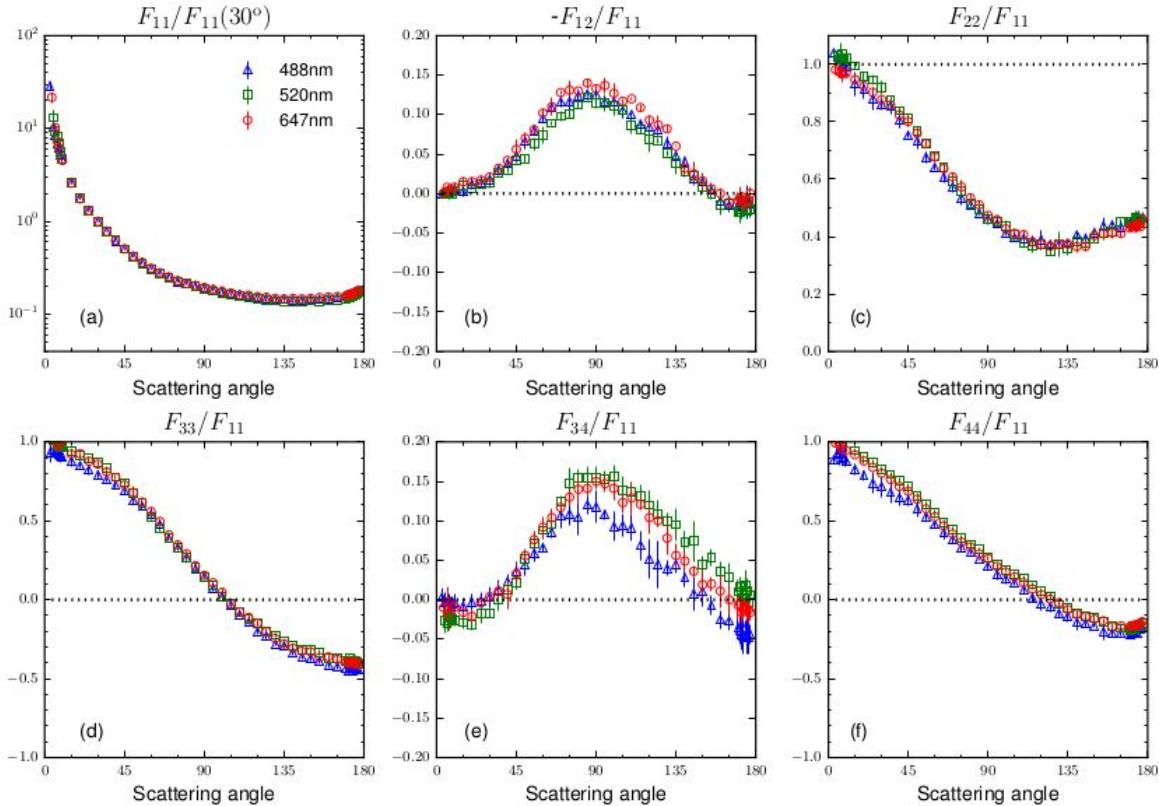
Escobar-Cerezo et al. (ApJSS, 2018)

JSC-1A SEM images

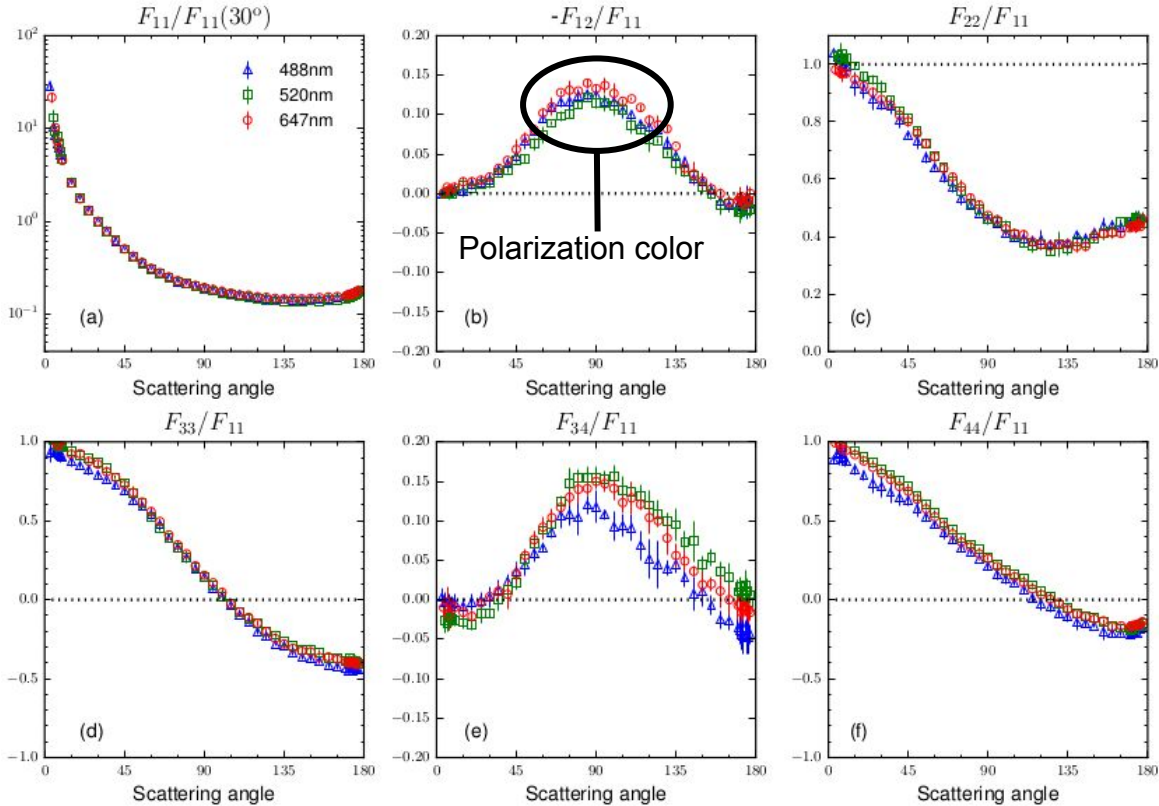


Escobar-Cerezo et al. (ApJSS, 2018)

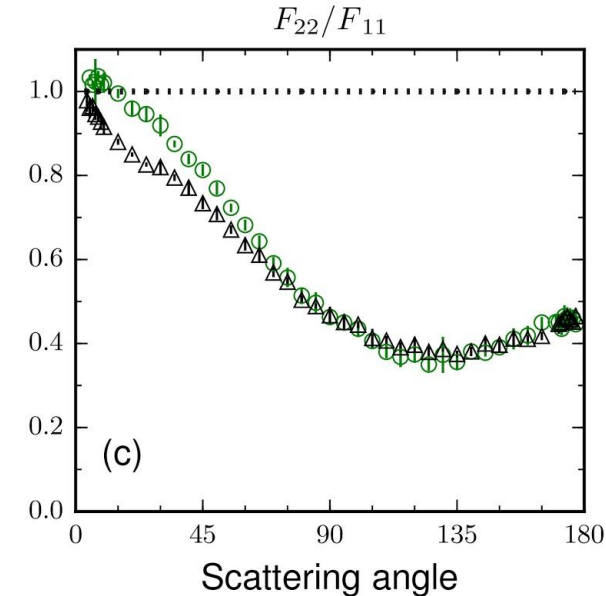
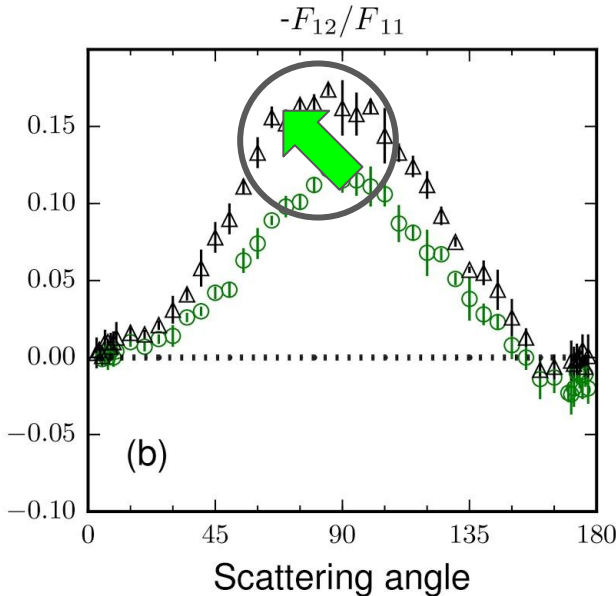
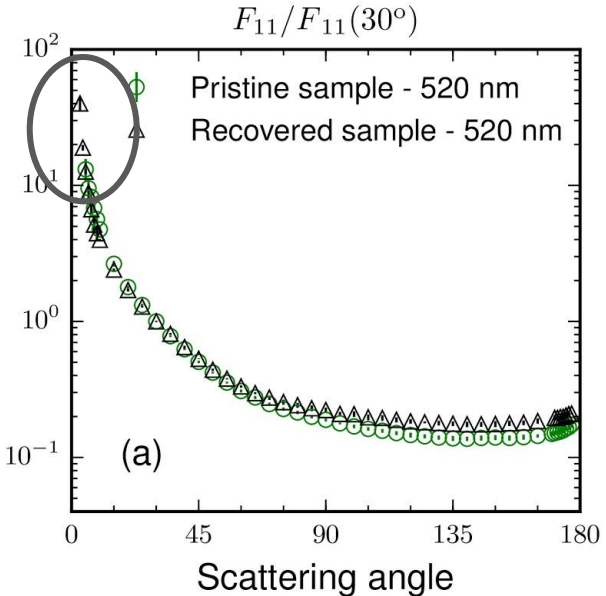
Experimental measurements of the JSC-1A lunar analog



Experimental measurements of the JSC-1A lunar analog



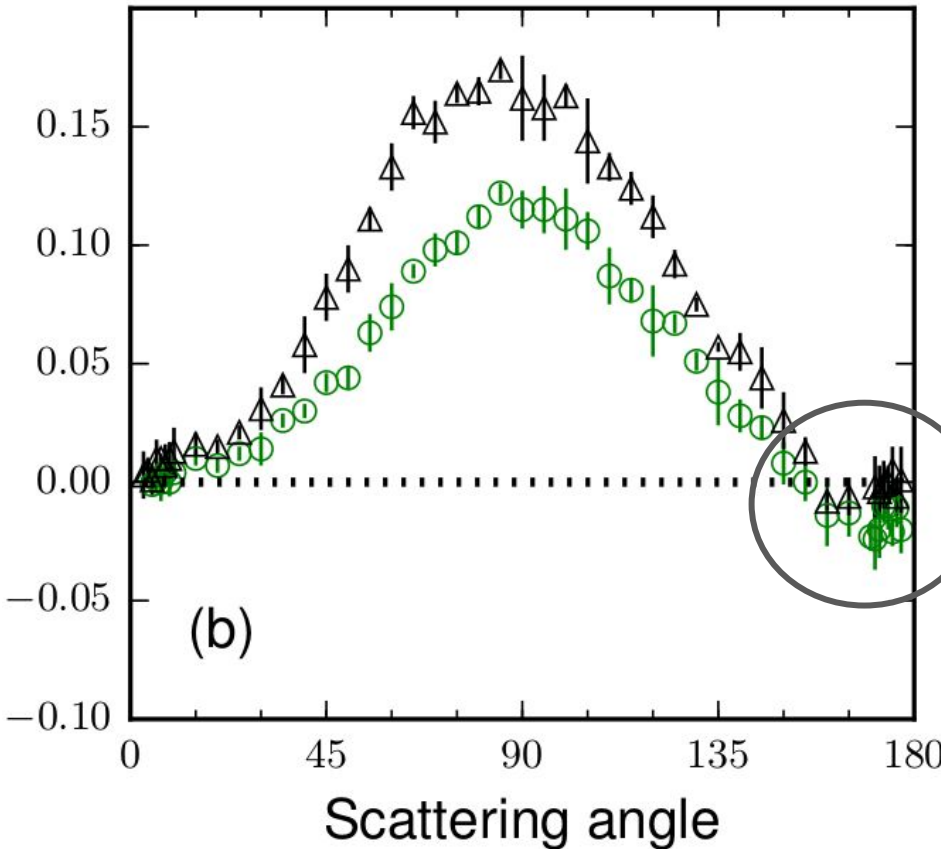
Comparing pristine and recovered sample



Escobar-Cerezo et al. (ApJSS, 2018)

Comparing pristine and recovered sample

$$-F_{12}/F_{11}$$

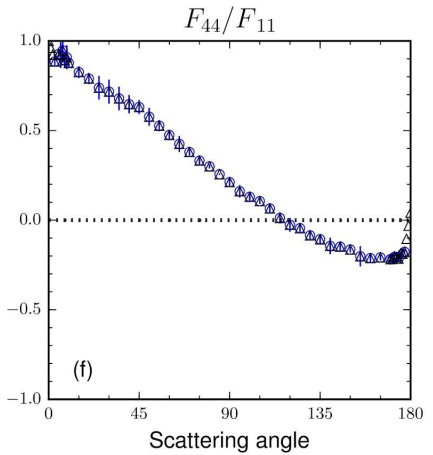
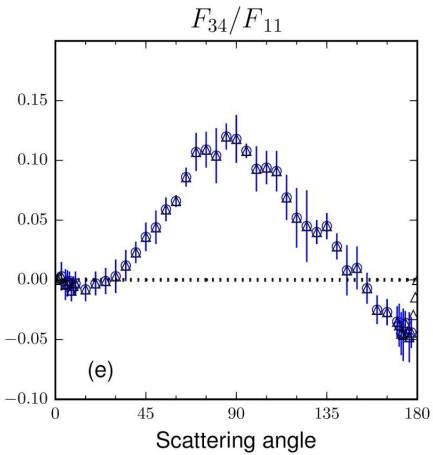
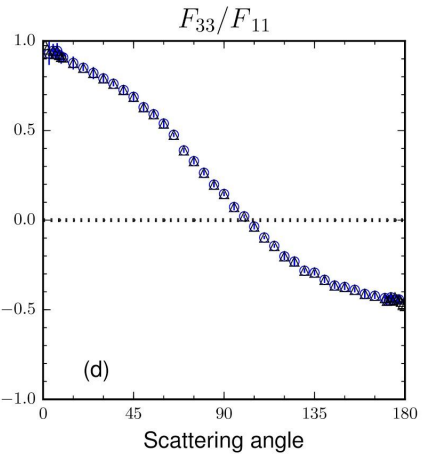
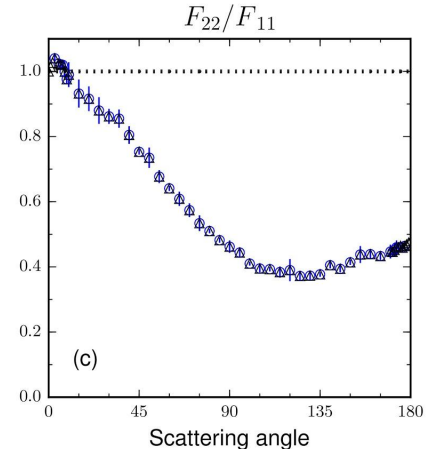
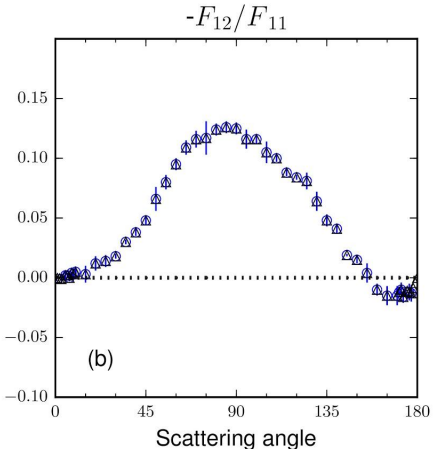
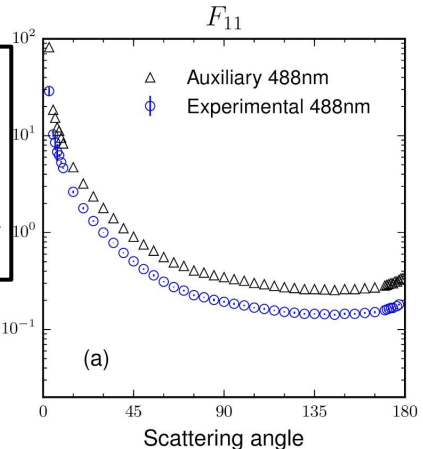


Submicron-size particles seem to be responsible for the measured negative branch !!!

Extrapolated matrix for JSC-1A lunar analog

Normalization condition

$$\frac{1}{2} \int_0^\pi d\theta \sin \theta F_{11}^{\text{syn}}(\theta) = 1$$



Computed asymmetry parameter and depolarization factor

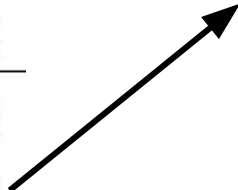
Asymmetry parameter g

Wavelength λ	Mie
488 nm	0.74
520 nm	0.75
647 nm	0.74

Back-scattering depolarization factor $\delta_L(180^\circ)$

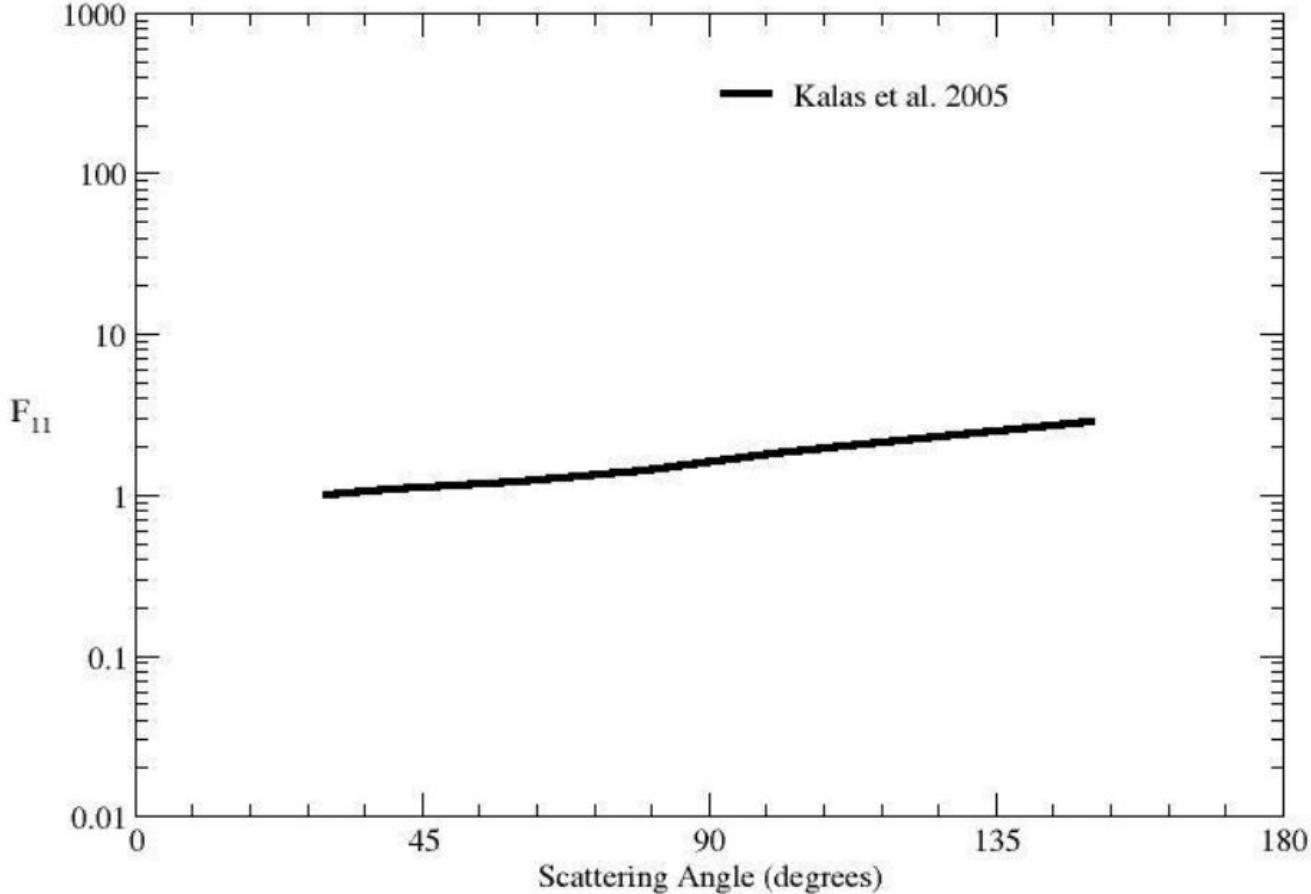
Wavelength λ	Mie
488 nm	0.35
520 nm	0.42
647 nm	0.31

Sterzik et al. assumed that the regolith depolarizes the light by a factor of 3.3 at 550nm (i.e. 0.3 as expressed on the table).



Experimental Phase Functions of Millimeter-sized Cosmic Dust Grains

Experimental Phase Functions of Millimeter-sized Cosmic Dust Grains



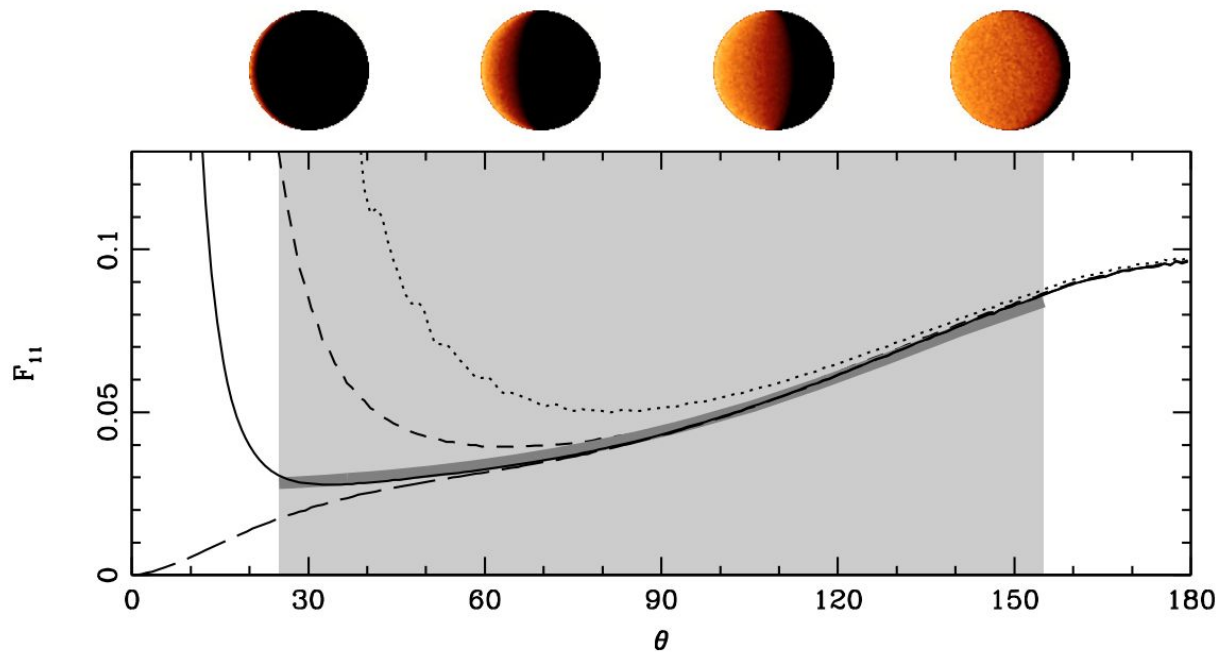
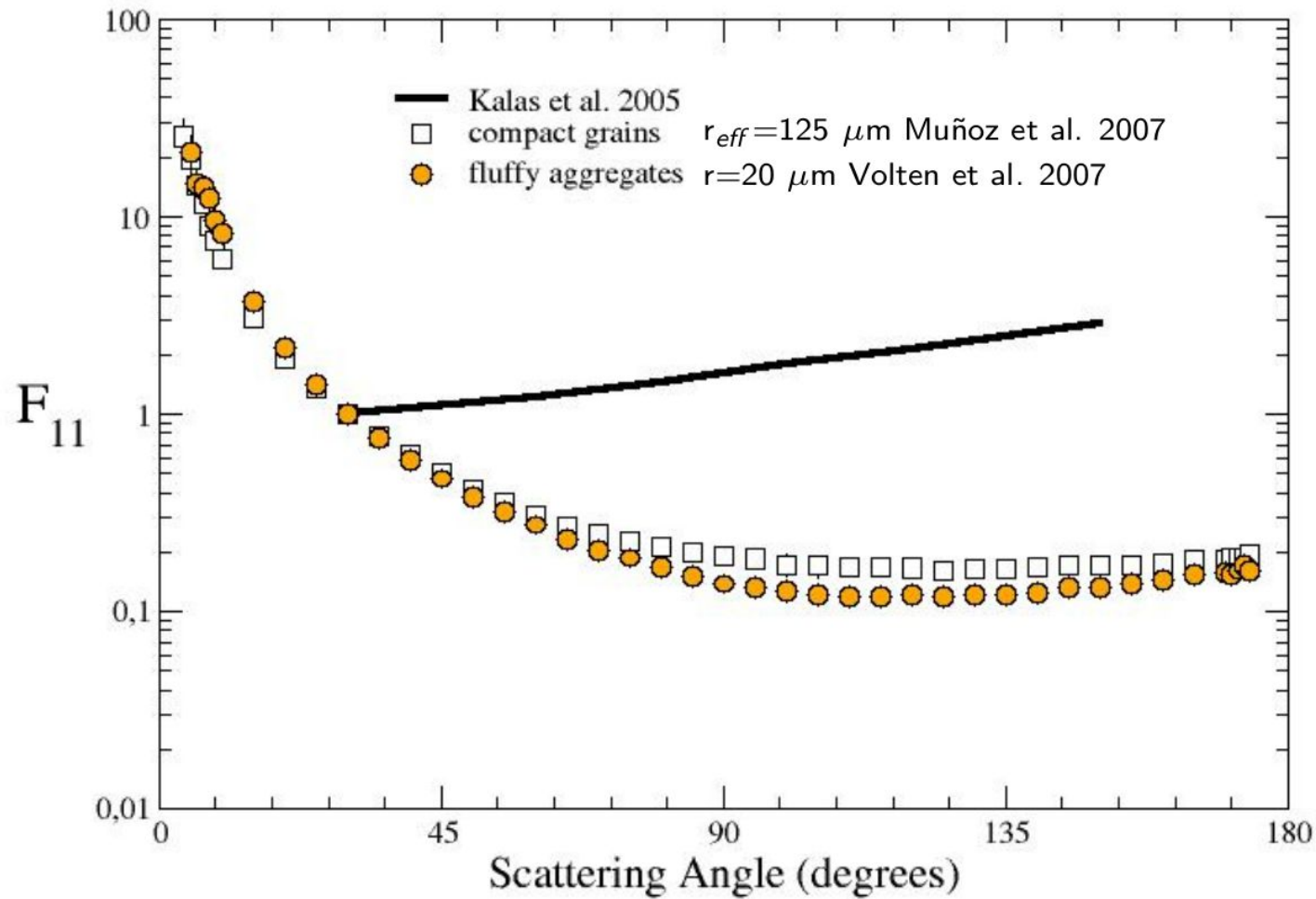


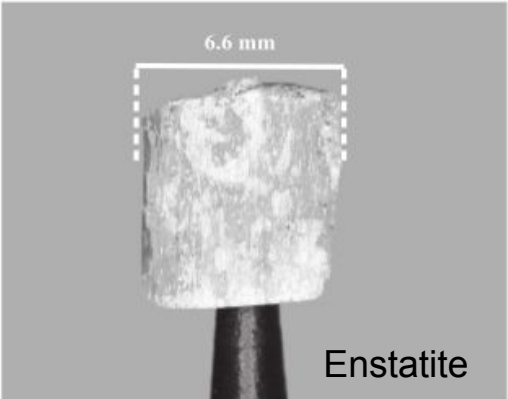
Fig. 2. Angular scattering functions for large dust grains, showing the relative intensity scattered at a scattering angle θ . The pure reflectance function (long-dashed curve) is given, and diffraction effects are added for 10, 30 and 100 μm grains (dotted, dashed and solid curves). The empirical scattering function of the Fomalhaut disk grains from [Kalas et al. \(2005\)](#) is also shown (thick grey curve, albedo chosen to match the computations). The grey area indicates the observable range of scattering angles for the Fomalhaut system.

- Very large grains ($>100 \mu\text{m}$) to explain HST images (Min *et al.* 2010).
- Fomalhaut: Herschel far-IR spectra shows high temperature grains.
- Large ($r \sim 15 \mu\text{m}$) fluffy aggregates consisting of small monomers to explain far-IR Herschel data. (Acke *et al.* 2012).

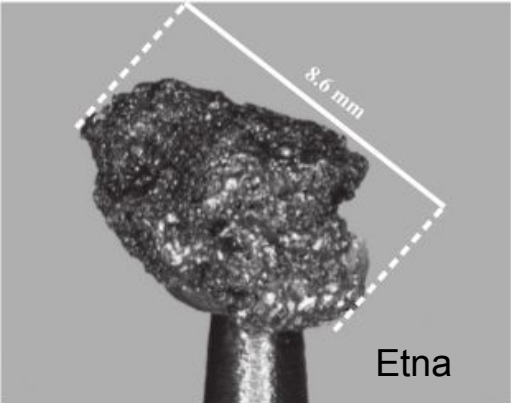


Experimental Phase Functions of Millimeter-sized Cosmic Dust Grains

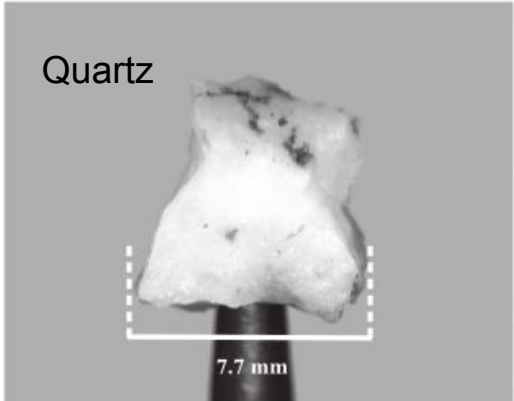
$$n=1.58 + i2.10^{-5}$$



$$n=1.59 + i0.01$$



Quartz

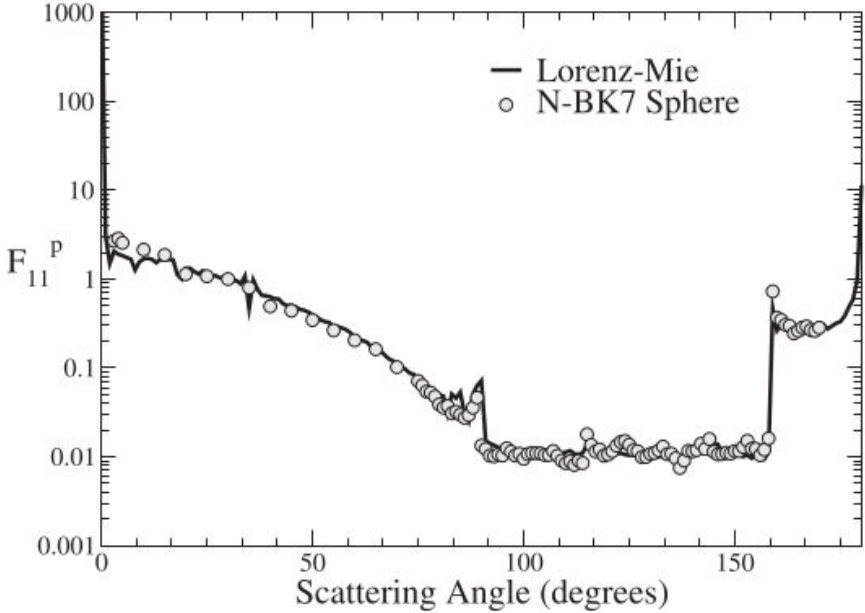


$$n=1.54 + i0.0$$

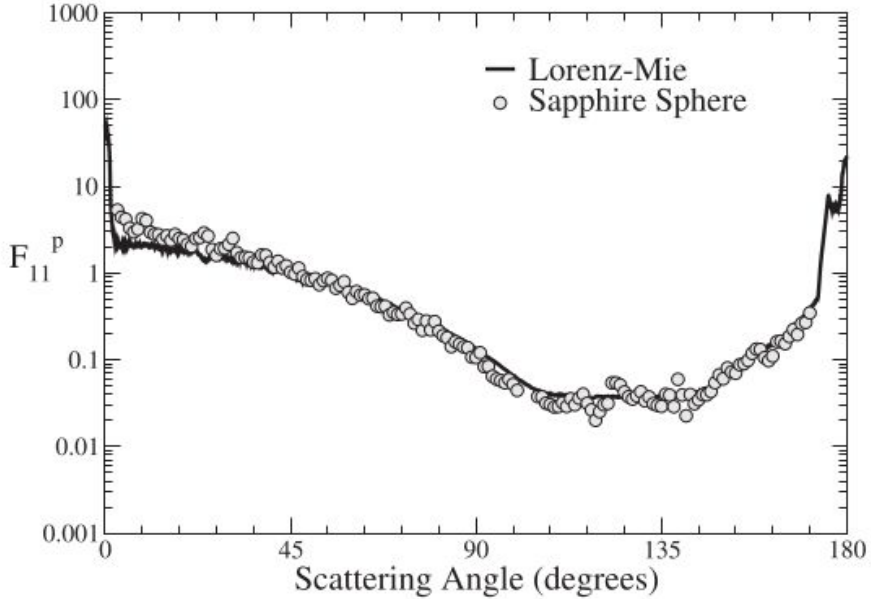
Muñoz et al. (2017)



Experimental Phase Functions of Millimeter-sized Cosmic Dust Grains



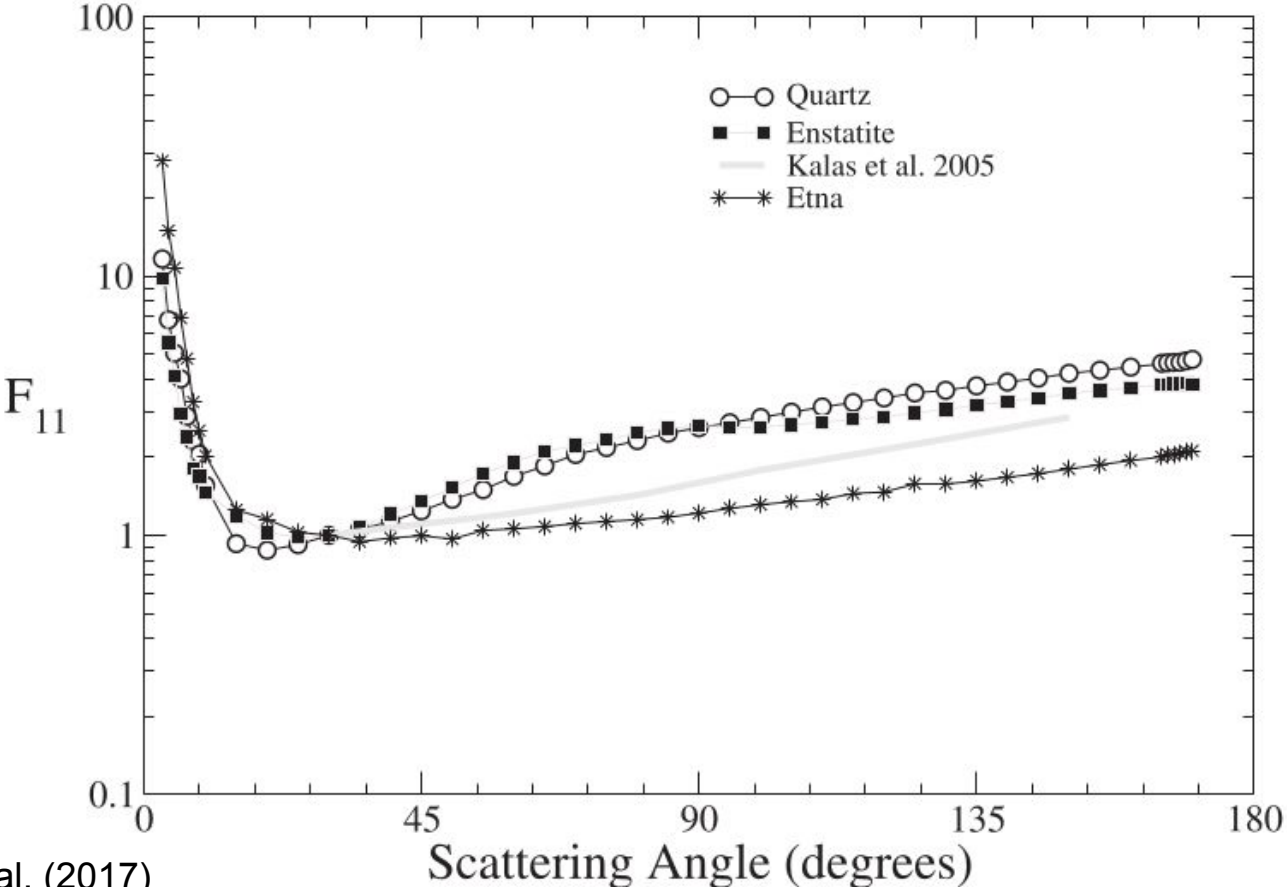
(a)



(b)

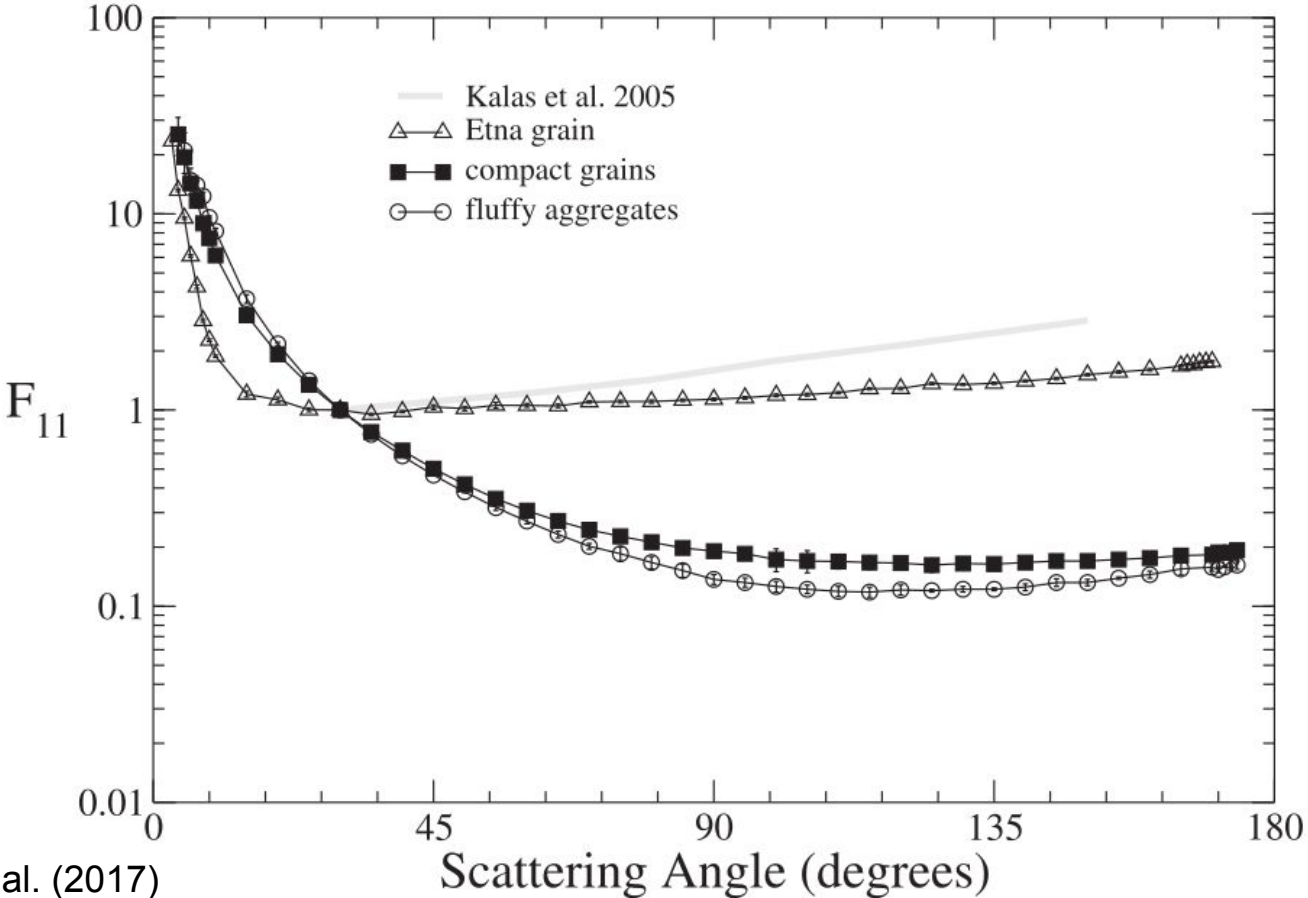
Muñoz et al. (2017)

Experimental Phase Functions of Millimeter-sized Cosmic Dust Grains



Muñoz et al. (2017)

Experimental Phase Functions of Millimeter-sized Cosmic Dust Grains



Muñoz et al. (2017)

Goniophotometers

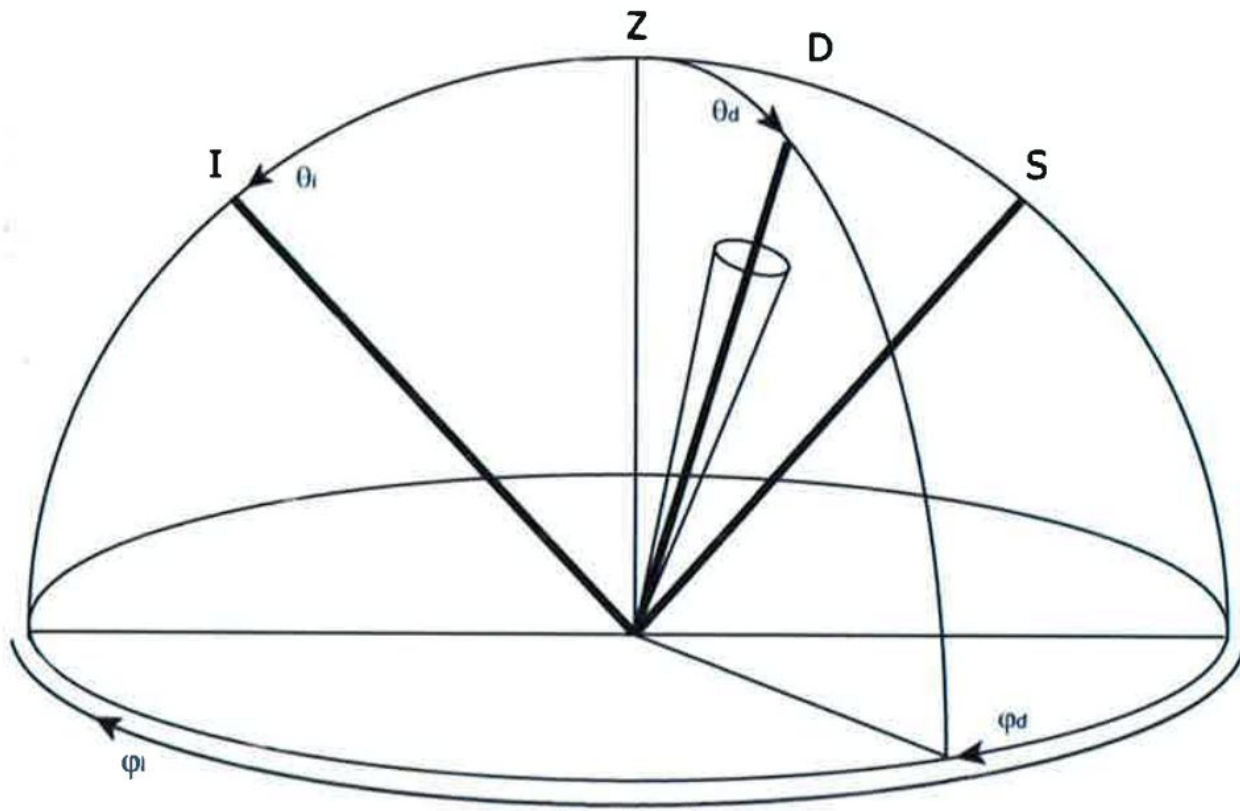
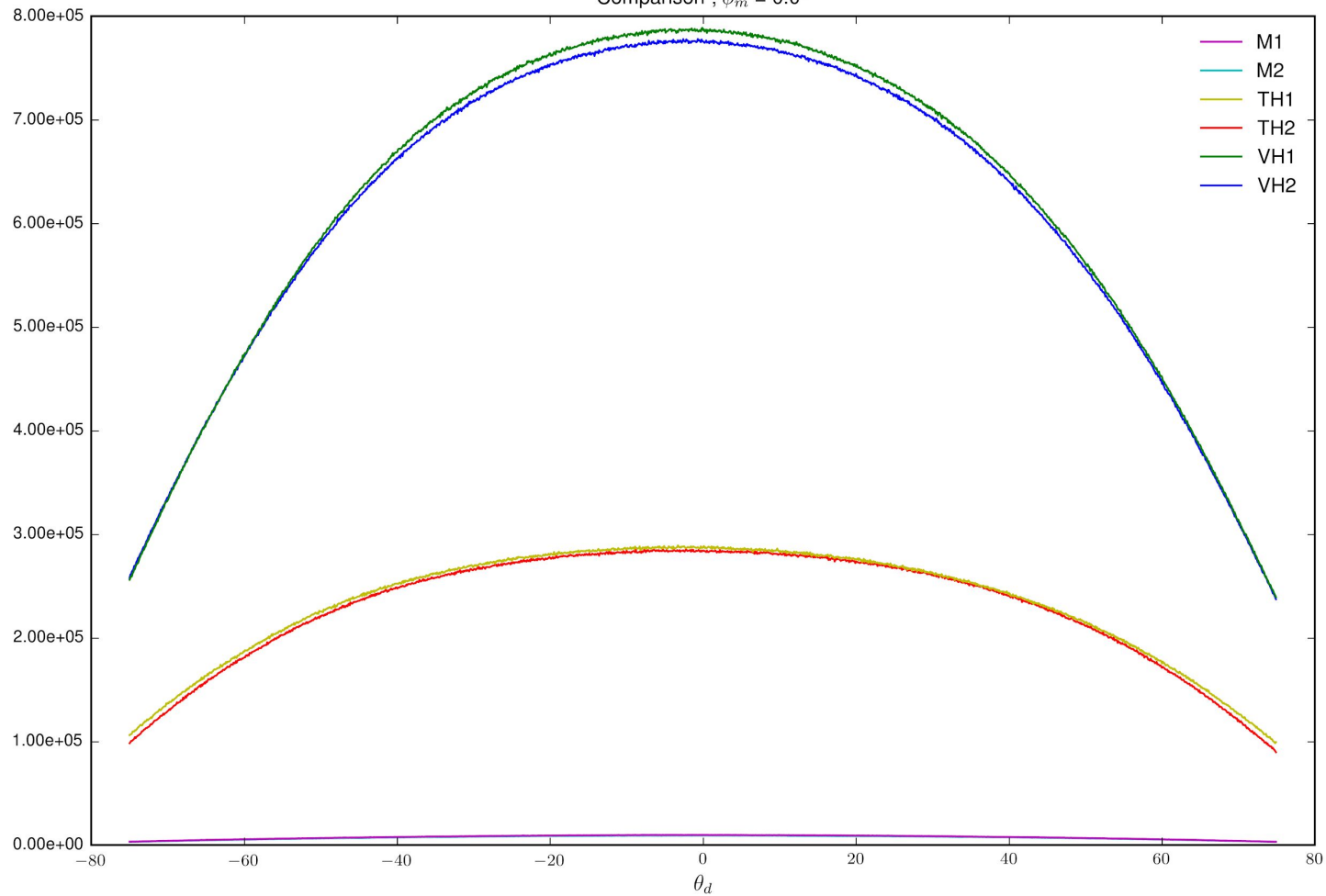
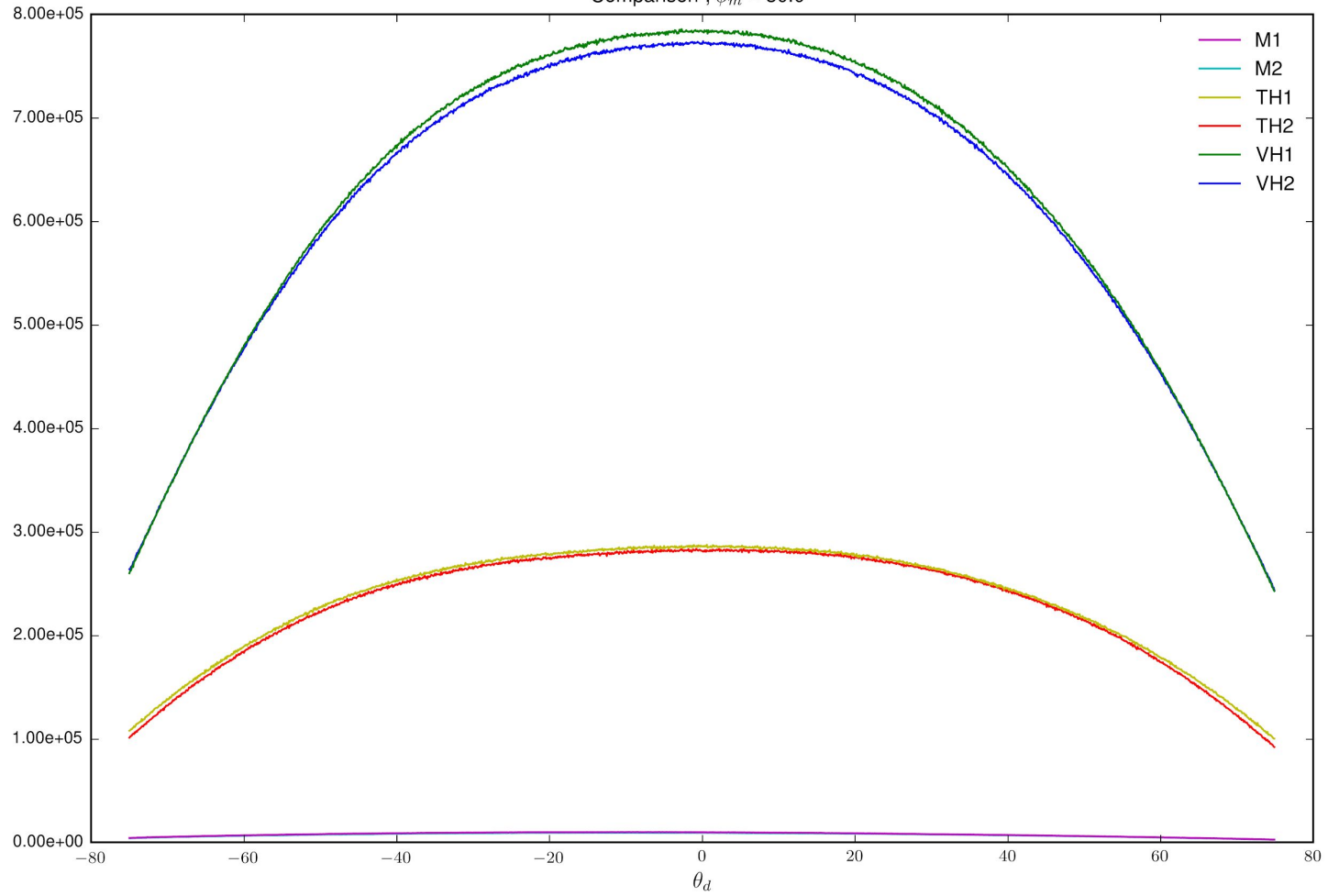


Fig. 1: Coordinate system

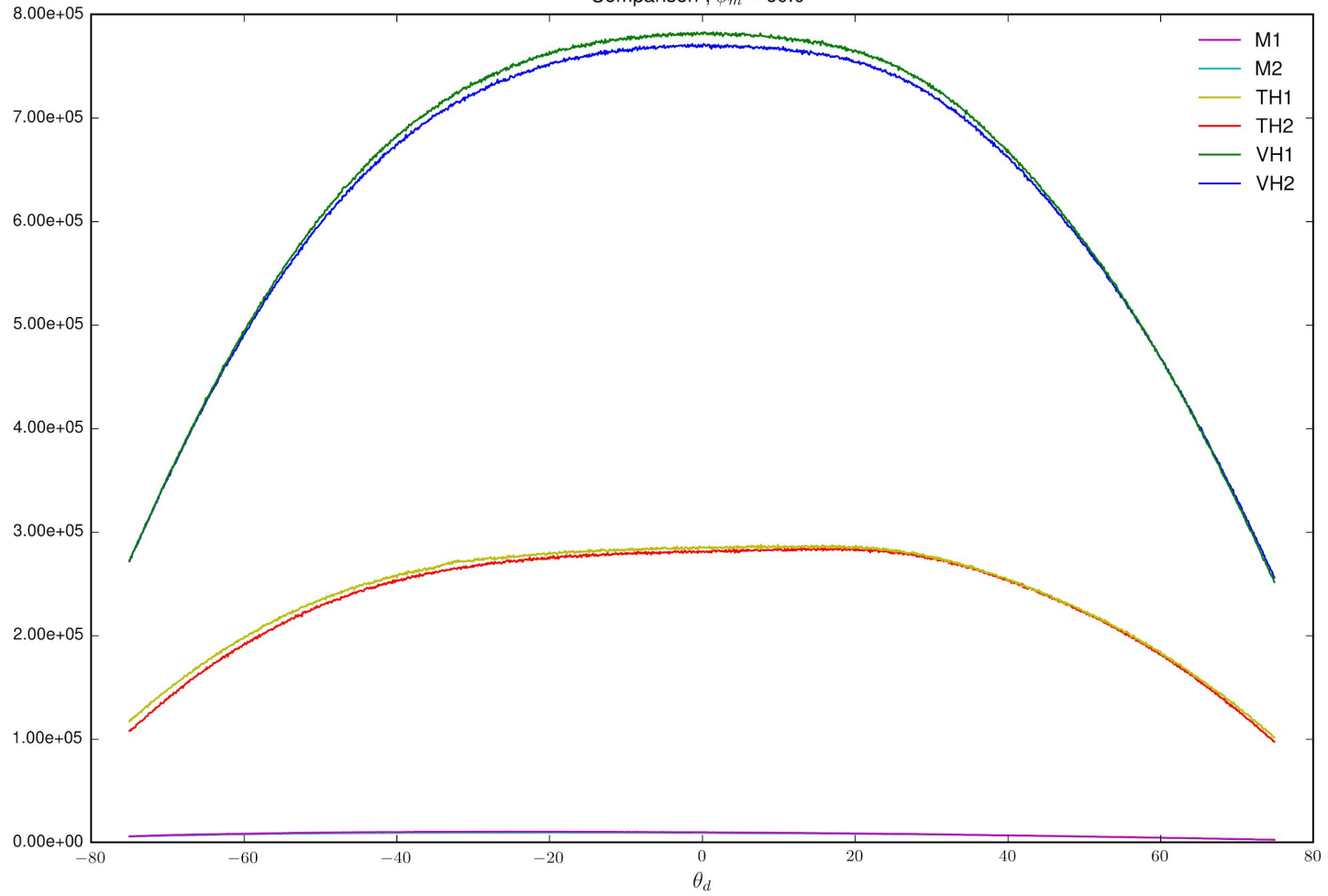
Comparison ; $\phi_m = 0.0^\circ$



Comparison ; $\phi_m = 30.0^\circ$



Comparison ; $\phi_m = 60.0^\circ$



Comparison ; $\phi_m = 90.0^\circ$

